Investigations on Bi25FeO40 powders synthesized by hydrothermal and combustion-like processes

Roberto Köferstein, Toni Buttlar, Stefan G Ebbinghaus

Journal of Solid State Chemistry 217 (2014) 50–56

(doi: 10.1016/j.jssc.2014.05.006)

http://dx.doi.org/10.1016/j.jssc.2014.05.006

Investigations on $Bi_{25}FeO_{40}$ powders synthesized by hydrothermal and combustion-like processes

Roberto Köferstein*, Toni Buttlar and Stefan G. Ebbinghaus

Institute of Chemistry, Inorganic Chemistry, Martin-Luther-University Halle-Wittenberg, Kurt–Mothes–Strasse 2, 06120 Halle, Germany.

* Corresponding author. Tel.: +49-345-5525630; Fax: +49-345-5527028.
E-mail address: roberto.koeferstein@chemie.uni-halle.de

Abstract. The syntheses of phase–pure and stoichiometric iron sillenite ($Bi_{25}FeO_{40}$) powders by a hydrothermal (at ambient pressure) and a combustion–like process are described. Phase–pure samples were obtained in the hydrothermal reaction at 100 °C (**1**), whereas the combustion–like process leads to pure $Bi_{25}FeO_{40}$ after calcination at 750 °C for 2 h (**2a**). The activation energy of the crystallite growth process of hydrothermally synthesized $Bi_{25}FeO_{40}$ was calculated as 48(9) kJ mol^{-1}. The peritectic point was determined as 797(1) °C. The optical band gaps of the samples are between 2.70(7) eV and 2.81(6) eV. Temperature and field–depending magnetization measurements (5–300 K) show a paramagnetic behaviour

with a Curie constant of $55.66 \cdot 10^{-6}$ $m^3 \cdot K \cdot mol^{-1}$ for sample **1** and $C = 57.82 \cdot 10^{-6}$ $m^3 \cdot K \cdot mol^{-1}$ for sample **2a** resulting in magnetic moments of $\mu_{mag} = 5.95(8)$ $\mu_B \cdot mol^{-1}$ and $\mu_{mag} = 6.07(4)$ $\mu_B \cdot mol^{-1}$. The influence of amorphous iron–oxide as a result of non-stoichiometric Bi/Fe ratios in hydrothermal syntheses on the magnetic behaviour was additionally investigated.

Keywords: *Iron sillenite; Combustion Synthesis; Magnetic properties; Amorphous oxides; Band gap; hydrothermal*

1. Introduction

Sillenite materials are of great importance because of their photorefractive, piezoelectric, electrooptic, and photoconductive properties [1,2,3]. $Bi_{25}FeO_{40}$ is a sillenite-type material which crystallizes in the cubic space group I23 with cell parameter of about 1.018 nm [4,5]. In the literature two possible chemical formulas $Bi_{25}FeO_{40}$ and $Bi_{25}FeO_{39}$ can be found [6,7]. *Craig* and *Stephenson* [4] have shown that one Bi ion per unit cell exists in the oxidation state +5 resulting in the formula $Bi^{III}_{24}(Bi^{V}Fe^{III})O_{40}$. Investigations by *Devalette* et al. [8], *Soubeyroux* et al. [9], and *Wang* et al. [10] also confirmed the formation of Bi^{5+}. In the sillenite structure of $Bi_{25}FeO_{40}$ the Bi^{3+} ions occupy the octahedral positions forming a cage of corner-connected BiO_5E–polyhedrons (E = inert $6s^2$ electron pair), whereas the Bi^{5+} and Fe^{3+} ions are sharing the tetrahedral positions within the cage [7,4]. On the other hand studies by *Radaev* et al. [11,12] suggest Bi^{3+} in the tetrahedral position accompanied by oxygen vacancies. In this paper we use the formula $Bi_{25}FeO_{40}$.

The magnetic properties of $Bi_{25}FeO_{40}$ samples prepared by soft–chemistry methods have been only rarely investigated and deviating results have been reported. *Cheng* et al. [13] found a paramagnetic–like behaviour at room temperature, whereas a superparamagnetic behaviour was also reported by other research groups [5,14,15,16]. In contrast a clear hysteresis loop at

room temperature was also found pointing to a ferro- or ferrimagnetic behaviour [17]. Additionally the values of the specific magnetization at room temperature vary significantly [5,13,14,15,17]. Moreover, a spin−glass freezing behaviour [17] as well as a possible ferromagnetic transition at low temperatures [5] were also reported. In contrast, magnetic measurements between 5 and 950 K on $Bi_{25}FeO_{40}$ powders prepared by the conventional mixed-oxide method show a paramagnetic behaviour [18,19,20]

$Bi_{25}FeO_{40}$ shows photocatalytic activity under ultraviolet and visible light irradiation in the degradation of methyl orange, methyl violet, and pentachlorophenol [15,21,22,23]. *Sun* et al. [24,16] used $Bi_{25}FeO_{40}$−graphene and $Bi_{25}FeO_{40}$−carbon-nitride composite materials for the degradation of methylene blue. It was reported that hydrothermally prepared $Bi_{25}FeO_{40}$ samples can be recycled by magnetic separation [15,16,24]. *Borowiec* et al. [25] found that single crystals of iron sillenite are strongly photochromic. Furthermore, $Bi_{25}FeO_{40}$ is a typical by−product in the synthesis of $BiFeO_3$ [26].

In addition to the classical solid state synthesis [7], various hydrothermal syntheses were performed to obtain $Bi_{25}FeO_{40}$ powders. The reported hydrothermal processes were mostly carried out with non−stoichiometric initial Bi/Fe ratios of 1, despite of the Bi/Fe ratio of 25 according to the chemical formula of iron sillenite [5,13,14,17,15,21,27,28]. A solvothermal synthesis by *Dai* and *Yin* [23] with an initial ratio of Bi/Fe = 24 led to $Bi_{25}FeO_{40}$ with small amounts of Bi_2O_3.

In this paper we present both a simple one-pot hydrothermal and a combustion-like synthesis of phase-pure $Bi_{25}FeO_{40}$ with an initial Bi/Fe ratio of 25. The hydrothermal process was carried out in aquous NaOH solution at 100 °C. For the combustion-like reaction starch was used as gellant and fuel, because starch is an eco-friendly and cheap abundant biopolymer. Phase evolution and the crystallite growth kinetics were monitored by XRD and the magnetic behaviour and the optical band gap were studied. Moreover, the influence of a non-

stoichiometric initial Bi/Fe ratio in the hydrothermal process on the magnetic properties was investigated.

2. Experimental

2.1. Material preparation

*$Bi_{25}FeO_{40}$ - Hydrothermal method at ambient pressure (sample **1**)*

The reaction was carried out in a PFA (perfluoroalkoxycoplomyer) round bottom flask in argon atmosphere to avoid the formation of carbonates and the leaching out of silicon from a glass flask. $Bi(NO_3)_3 \cdot 5H_2O$ (0.012 mol, *Alfa Aesar*) and $Fe(NO_3)_3 \cdot 9H_2O$ (0.00048 mol, *Merck*) were dissolved in 10 ml water and 1 ml HNO_3 (65 %). 70 ml of a 10 M NaOH was heated to about 80 °C and the ($Bi_{25}Fe$)−solution was added slowly. The resulted solution was refluxed for 6 h at ambient pressure under vigorous stirring. Afterwards the resulting yellow precipitate was filtered, washed with deionized water several times and dried at 120 °C for 2 h. The product is denoted as powder **1** in the following. Chemical analyses of the product (photometry (Merck Spectroquant iron test kit), complexometry [29]) results in a iron content of 9.35 mg per gram of sample and a bismuth content of 881.03 mg per gram sample indicating a molar Bi/Fe ratio of 25.2 (calc. 25).

*$Bi_{25}FeO_{40}$ - Combustion method (sample **2**)*

$Bi(NO_3)_3 \cdot 5H_2O$ (0.012 mol, *Alfa Aesar*) and $Fe(NO_3)_3 \cdot 9H_2O$ (0.00048 mol, *Merck*) were dissolved in 1 ml HNO_3 (65 %) and 10 ml deionized water. Then 2.0 g soluble starch (*Sigma−Aldrich*) was added and the resulting turbid solution was continuously stirred (if required under heating to about 35 °C) until it became a high viscous colourless gel. The ($Bi_{25}Fe$)−gel was calcined in static air at various temperatures up to 750 °C with a rate of 5 K

min^{-1}. Chemical analyses of a sample calcined at 750 °C for 2 h (powder **2a**), indicated a Bi/Fe ratio of 24.5.

*$Bi_{25}FeO_{40}$ - Hydrothermal method (sample **3**)*

The synthesis is similar to the hydrothermal method for sample **1**. However, an initial Bi/Fe ratio of 1 (0.006 mol $Bi(NO_3)_3 \cdot 5H_2O$ and 0.006 mol $Fe(NO_3)_3 \cdot 9H_2O$) and a 2 M NaOH solution was used. The sample is denoted as powder **3**.

*Amorphous iron- oxide - Hydrothermal method (sample **4**)*

Powder **4** was synthesized analogous to powder **1** using only 0.012 mol $Fe(NO_3)_3 \cdot 9H_2O$.

2.2. Characterization

X−ray powder diffraction patterns were collected at room temperature on a *Bruker D8−Advanced* diffractometer, equipped with a one−dimensional silicon strip detector (LynxEye™) and operating with Cu−K_α radiation. Powder patterns were refined both with the *Rietveld* program FullProf [30] and the profile fitting software PowderCell [31]. The volume−weighted average crystallite sizes were determined from the XRD line broadening using the *Scherrer* equation [32] and the integral peak breadth. The pseudo−Voigt function was used to model the peak profile of the reflections and the contribution of the strain-broadening was taken into account (software suite WinXPOW [33]). ATR (attenuated total reflection) Fourier transformed infrared (FT−IR) spectra were collected at room temperature using a *Bruker* Tensor 27 spectrometer equipped with a diamond ATR unit. SEM images were recorded with a *Philips* XL30 ESEM (Environmental Scanning Electron Microscope). Magnetic measurements were carried out using a *Quantum Design* PPMS 9. Hysteresis loops

were taken at 300 K and 5 K with magnetic field cycling between $\mu_0 H = -9$ and +9 T. In addition, the temperature dependent magnetizations were measured at $\mu_0 H = 0.1$ T in the temperature range of 5 to 300 K using field−cooled (FC) and zero−field cooled (ZFC) conditions. The samples were enclosed in gel capsules whose small contribution to the measured magnetic moment was subtracted before data evaluation. All magnetic values are given in SI units [34]. Diffuse reflectance spectra were recorded at room temperature using a *Perkin Elmer* UV−Vis spectrometer Lambda 19. $BaSO_4$ was used as white standard.

3. Results and discussion

3.1. Phase evolution and morphology

Hydrothermal process

Fig. 1a shows the XRD pattern of the yellow powder **1** synthesized by the hydrothermal method. The pattern shows only reflections of $Bi_{25}FeO_{40}$ [35] and no secondary phases were observed. The volume-weighted average crystallite size (size of a coherent scattering domain) was calculated as 75 nm. SEM images (Fig. 2a) reveal an agglomerated nature of powder **1**. Agglomerates up to 30 µm with a tetrahedron-like shape can be observed, which consist of smaller particles between 0.2 µm and 2 µm. Thermal treatment of powder **1** up to 750 °C for 2 h (rate 5 K min^{-1}) results in an increase of the crystallite size up to 159 nm (see inset in Fig. 3b).

The kinetics of crystallite growth during the thermal treatment of powder **1** can be expressed by the following phenomenological equation (1) [36]:

$$D^n - D_0^{\,n} = kt \cdot e^{\frac{-E_A}{RT}} \qquad (1)$$

where D_0 is the initial crystallite size (75 nm, powder **1**), D the crystallite size after calcination for the time t and at temperature T, k is the pre−exponential constant, n the

crystallite growth exponent, E_A the activation energy for the crystallite growth process and R the universal gas constant. From the inverse slope of $\ln(D-D_0)$ vs. $\ln t$ the kinetic crystallite growth exponent n can be calculated. For this purpose the crystallite sizes of powder **1** after heat treatment at 400 °C for different times from 2 h up to 140 h were determined (Fig. 3a). The crystallite growth exponent was found to be n = 3.4. The activation energy of the crystallite growth process was calculated as E_A = 48(9) kJ mol^{-1} from the slope of an *Arrhenius* plot ($\ln(D^{3.4}-D_0^{3.4})/t$ *vs.* $1/T$) as shown in Fig. 3b.

Moreover, the colour of the samples changes with increasing temperature treatment. While the as-prepared powder **1** has a yellow colour, we found that after heat treatment for 2 h at 600 °C the colour changes to permanent green-grey. A prolonged heating time up to 15 h leads to a green-grey powder even at 400 °C . In addition the colour of powder **1** turns to green-grey when it is irradiated by sunlight for some days at room temperatures. As seen in Fig. 1b and 1c the XRD patterns after heating or sunlight exposure do not differ from powder **1**. In table 1 the thermal treatment, crystallite sizes and cell parameters of selected samples are listed.

Combustion-like process

Fig. 4 shows the phase evolution during the thermal decomposition of the colourless ($Bi_{25}Fe$)-gel. The gel was heated in static air with a rate of 5 K min^{-1} and a soaking time of 2 h. As shown elsewhere [37] the decomposition of the ($Bi_{25}Fe$)-gel is a combustion-like reaction in which the starch acts as fuel and the nitrate ions as oxidizer. Heating at 300 °C (Fig. 4a) results in a yellow-brown powder showing reflections of monoclinic and tetragonal Bi_2O_3 and $Bi_2O_2CO_3$ [35]. The yellow-ochre sample after calcination at 400 °C reveals traces of $Bi_2O_2CO_3$ and the formation of $Bi_{25}FeO_{40}$ [35] (Fig. 4b). A mixture of monoclinic Bi_2O_3 and $Bi_{25}FeO_{40}$ can be found in the dark-yellow samples after heating at 500 and 600 °C (Fig. 4c). At 700 °C the colour turns to green-grey and the pattern shows the presence of $Bi_{25}FeO_{40}$ and

only small amounts (3 wt%) of Bi_2O_3 (Fig. 4d). Phase pure green-grey $Bi_{25}FeO_{40}$ powder was obtained after heating at 750 °C (powder **2a**, Fig. 4e). A prolonged soaking time of 10 h at 700 °C (Fig. 4f) also results in a single-phase sample (powder **2b**). The volume-weighted average crystallite sizes of powders **2a** and **2b** were found to be 111 nm and 128 nm. REM images of powder **2a** show irregular agglomerates up to 60 µm of particles between 0.4 µm and 3 µm (Fig. 2b).

The XRD patterns (Fig. 5) were refined on the basis of a body-centred cubic unit cell (space group: I23) according to *Infante* and *Carrasco* [38]. The cubic lattice parameter for powder **2a** from the combustion process (calcined at 750 °C/ 2h) was calculated as a = 1.01859(3) nm and agrees well with previously reported data [5,38]. The unit cell parameter for the hydrothermally synthesized sample **1** is slightly larger (a = 1.01990(1) nm), whereas heat treatment of powder **1** at 750 °C for 2 h (powder **1d**) results in a slightly smaller lattice parameter of a = 1.01897(1) nm. The slightly larger unit cell of **1** may be explained by hydroxyl groups inside the lattice, which was found in e.g. perovskites prepared by hydrothermal routes and organic coordination precursors [39,40].

The IR spectra (ATR technique) of the hydrothermal powders **1** (as-prepared), **1d** (annealed at 750 °C), and powder **2a** from the combustion syntheses calcined at 750 °C are shown in Fig. 6. The samples show the three typical absorption bands for sillenites stemming from the Bi–O framework [18,38]. Powders **1d** and **2a** reveal bands at 576, 523 and 457 cm^{-1}. On the other hand the vibration bands of the as-prepared powder **1** are slightly shifted to 575, 516, and 446 cm^{-1}. Keeping powder **1** in sunlight for some days (Fig. 5b) results in an identical IR spectrum.

$Bi_{25}FeO_{40}$ is an incongruent melting compound [41,42]. Its melting temperature was determined by the onset of the DTA signal during the heating phase [43] of powder **1** (hydrothermal) and powder **2a** (combustion process). The melting temperature (peritectic point) of both samples was observed at 797(1) °C and agree very well with the values of 795 °C and 798 °C reported by *Kargin* and *Skorikov* [41] and *Maître* et al. [42], respectively.

3.2. Diffuse reflectance spectra

Fig. 7a shows the diffuse reflectance spectra of powders **1** and **2a**, respectively. The *Kubelka–Munk* function (2) [44] was used for analysis of the spectra (see Fig. 7b).

$$F(R) = \frac{\alpha}{s} = \frac{(1-R)^2}{2R} \quad (2)$$

where $F(R)$ is the *Kubelka–Munk* function, R the reflectance, α the absorption coefficient and s is the scattering factor. Since the scattering factor is wavelength independent, $F(R)$ is proportional α [45]. The absorption coefficient α is connected with the band gap energy according to equation 3 [46].

$$\alpha h\nu = k(h\nu - E_g)^{1/n} \quad (3)$$

where k is an energy–independent constant, E_g the optical band gap. The exponent n is determined by the type of transition (n = 2 direct allowed, n = 0.5 indirect allowed). Assuming a direct allow transition in accordance with earlier investigations [14,15,21], the optical band gap (E_g) can be determined by plotting $(F(R)\cdot h\nu)^2$ vs. $h\nu$ and extrapolating the slope to $F(R) \rightarrow 0$ (inset in Fig. 6b). The yellow hydrothermally synthesized powder **1** has a band gap of 2.73(7) eV and heating to 750 °C (powder **1d**, green–grey) does not change this value (2.71(8) eV). After keeping powder **1** in sunlight for 10 days the resulting green–grey powder reveals a band gap of 2.70(8) eV. The origin of the colour change of powder **1** has not

yet been identified and is a subject for further investigations. The phase–pure sample **2a** from the combustion–like process calcined at 750 °C reveals a band gap value of 2.81(6) eV. *Senuliene* et al. [47], *Borowiec* [48], *Kargin* and *Skorikov* [41], and *Zhang* et al. [21] reported values of 2.8 eV and 2.4 eV. On other hand, band gap values between 1.68 eV and 2.0 eV were also reported [14,15,24,27]. The broad variation of the optical band gaps is most likely caused by different techniques to determine the band gap [49], different syntheses or different particle sizes. Additionally, most of the reported syntheses use a non–stoichiometric initial mixture of bismuth and iron salts (excess of Fe–ions) resulting in brown powders [13,21].

3.3. Magnetic measurements

The magnetic behaviour of the $Bi_{25}FeO_{40}$ samples is demonstrated in Fig. 8 for powder **2a**. The magnetic susceptibility was measured between 5 and 300 K after cooling the sample in zero applied magnetic field (ZFC) and an external magnetic field of $\mu_0 H$ = 0.1 T (FC). The ZFC curve and the FC curve are almost identical. The development of magnetization (M) depending on the applied magnetic field (H) at 300 K is shown in the inset of Fig. 8. The magnetization increases linearly with the applied field and no hysteresis loop is observed. The temperature dependence of the susceptibility can be fitted by a modified Curie–Weiss law (4) [50]

$$\chi_{mol} = \frac{C}{T - \Theta} + \chi_0 \quad (4)$$

where C is the Curie constant, T the temperature, Θ the Weiss constant and χ_0 is a temperature independent term. For powder **1** and **2a** Θ is −5.66 K and −3.21 K and χ_0 is $0.016 \cdot 10^{-6}$ $m^3 \cdot mol^{-1}$ and $0.061 \cdot 10^{-6}$ $m^3 \cdot mol^{-1}$, respectively, indicating a small temperature-independent paramagnetic component. The Curie constants were refined as $C = 55.66 \cdot 10^{-6}$ $m^3 \cdot K \cdot mol^{-1}$ (**1**) and $C = 57.82 \cdot 10^{-6}$ $m^3 \cdot K \cdot mol^{-1}$ (**2a**), which are close to the values for $Bi_{25}FeO_{40}$ synthesized by the conventional mixed–oxide method [18,19,20]. From the Curie constants we calculated

magnetic moments for powder **1** and **2a** as μ_{mag} = 5.95(8) $\mu_B \cdot mol^{-1}$ and μ_{mag} = 6.07(4) $\mu_B \cdot mol^{-1}$, respectively. These values agree well with the theoretical spin–only value of 5.92 μ_B for Fe^{3+} in a tetrahedral crystal field .

3.4. Influence of amorphous iron-oxde

We suppose that the finding of superparamagnetism, hysteresis loops and magnetic transitions at low temperatures (irreversibility of the ZFC–FC curves) in $Bi_{25}FeO_{40}$ samples prepared by hydrothermal methods [5,13,14,15,16,17,] is caused by X–ray amorphous iron–oxide or iron–rich species as secondary phases, because of the non–stoichiometric initial Bi/Fe ratios. To investigate the appearance of the reported superparamagnetism and magnetic transitions, we hydrothermally synthesized $Bi_{25}FeO_{40}$ with an initial Bi/Fe ratio of 1 (sample **3**) and pure X–ray amorphous iron–oxide (sample **4)**.

Sample **3** was prepared by reacting of $Bi(NO_3)_3 \cdot 5H_2O$ and $Fe(NO_3)_3 \cdot 9H_2O$ with a Bi/Fe ratio of 1 in a 2 M NaOH solution at 100 °C. The obtained brown powder shows only reflections corresponding to $Bi_{25}FeO_{40}$. The increased background level at lower diffraction angles, primarily in the range 2θ = 25–40°, suggests the presence of an amorphous fraction (Fig. 9a). Heating the sample to 750 °C for 2 h leads to the formation of $Bi_2Fe_4O_9$ (Fig. 9b) and proves that powder **3** contains amorphous iron–oxide. The temperature–dependent magnetization shows a separation of the ZFC curve from the FC curve as shown in Fig. 10a. The FC curve increase with decreasing temperature, while the ZFC curve has maximum at about 25 K. Below this temperature the ZFC curve starts to decrease. The field–dependent magnetization at 300 K (Fig. 10b) indicates a typical superparamagnetic behaviour [51,52], whereas measurements at 5 K result in the formation of pronounced hysteresis loops with a coercivity value of $\mu_0 H_c = 52 \cdot 10^{-4}$ T.

Powder **4** was obtained after hydrothermal reactions of $Fe(NO_3)_3 \cdot 9H_2O$ in 10 M NaOH solution, respectively. The XRD pattern shows the X–ray amorphous nature (Fig. 9c) of the powder, only the weak reflections at 2θ = 33.2 and 35.7° suggest the formation of Fe_2O_3 (hematite) [35] with a very poor crystallinity. The sample shows a superparamagnetic behaviour at 300 K (Fig. 11b). Analogous to powder **3** we find a separation of the FC and ZFC curves with a maximum at 50 K under ZFC conditions (Fig. 11a). That maximum is the so–called blocking temperature (T_B) and reflects the transition between the superparamagnetic state (above T_B) and the ferro– or ferrimagnetic state (below T_B) [53,54]. The blocking temperature depends on the particle size and the applied magnetic field. Field–dependent measurements below the blocking temperature reveal the formation of pronounced hysteresis loops (inset in Fig. 11b) in agreement with earlier reports on amorphous iron–oxides [55,56,57,58].

Based on these findings we conclude that the reported superparamagnetic behaviour of hydrothermally synthesized iron-sellinite powders is not a property of $Bi_{25}FeO_{40}$ but is caused by amorphous iron–oxide species within the samples, due to the non–stoichiometric initial Bi/Fe ratios. Additionally, the reported magnetic transitions at low temperatures can be interpreted as the transition between the superparamagnetic and the ferro– or ferrimagnetic state of amorphous iron–oxides. Moreover, the presence of amorphous iron–oxide in powder **3** explains the decreasing band gap value of 2.20(2) eV.

Conclusion

Stoichiometric $Bi_{25}FeO_{40}$ powders were synthesized both by a simple hydrothermal synthesis at 100 °C and by a combustion–like reaction using starch as a complexing agent and gellant. The hydrothermal synthesis leads to a yellow sample (powder **1**) showing only reflections of

$Bi_{25}FeO_{40}$. The colour of the powder changes to permanent green−grey upon irradiation with sunlight at room temperature or heating to at least 400 °C. The combustion−like process leads to phase−pure $Bi_{25}FeO_{40}$ after calcining the ($Bi_{25}Fe$)−gel at 750 °C for 2 h (powder **2a**) or at 700 °C for 10 h. The calculated volume−weighted crystallite sizes range from 75 to 159 nm depending on the synthesis and heat treatment. REM investigations show highly agglomerated powders. The optical band gaps were found to be between 2.70(7) eV and 2.81(6) eV. Magnetic measurements between 5 and 300 K show a paramagnetic Curie-Weiss behaviour with Curie constants of $55.66 \cdot 10^{-6}$ $m^3 \cdot K \cdot mol^{-1}$ (powder **1**) and $57.82 \cdot 10^{-6}$ $m^3 \cdot K \cdot mol^{-1}$ (powder **2a**) resulting in magnetic moments of $\mu_{mag} = 5.95(8)$ $\mu_B \cdot mol^{-1}$ (**1**) and $\mu_{mag} = 6.07(4)$ $\mu_B \cdot mol^{-1}$ (**2a**), respectively. We are able to prove that the finding of superparamagnetism, hysteresis loops and magnetic transitions for hydrothermally synthesized samples reported in literature is most probably caused by X−ray amorphous iron−oxide, which is formed as a by−product because of non−stoichiometric initial Bi/Fe ratios.

Acknowledgements

Financial support by the German Science Foundation within the Collaborative Research Centre (SFB 762) *Functionality of Oxide Interfaces* is gratefully acknowledged.

Tab. **1**: Preparation, colour, crystallite size, and cell parameter for selected phase-pure $Bi_{25}FeO_{40}$ samples

Powder	Heat treatment (rate 5 K min^{-1})	Colour	d_{cryst} (nm)[1)]	Unit cell parameter (nm)[2)]
Hydrothermal synthesis				
1	–	yellow	75	1.01990(1)
1a	300°C, 2h	yellow	77	
1b	400°C, 2h	yellow [3)]	81	
1c	600°C, 2h	green-grey	95	
1d	750°C, 2h	green-grey	159	1.01897(1)
Combustion synthesis				
2a	750°C, 2h	green-grey	111	1.01859(3)
2b	700°C, 10h	green-grey	128	

1) volume-weighted-crystallite size
2) cubic unit cell
3) green-grey after a heating time of 15 h

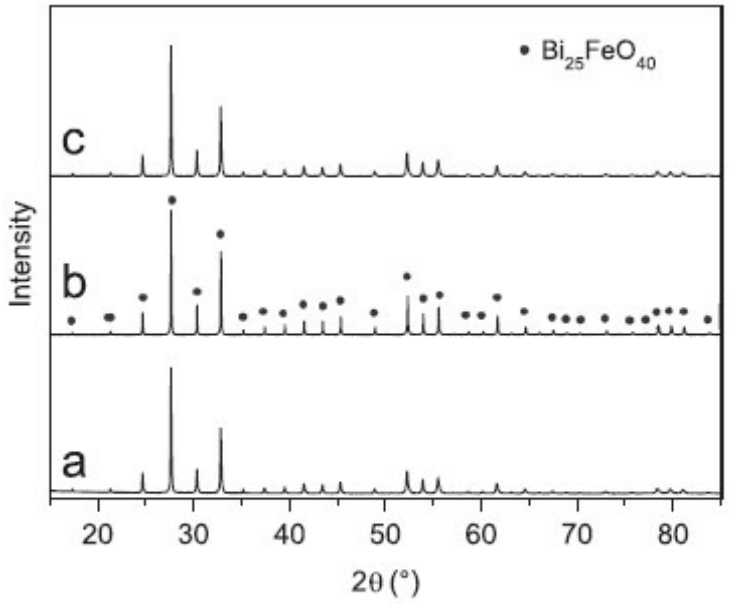

Fig. 1. Room temperature XRD patterns of hydrothermally synthesized $Bi_{25}FeO_{40}$. (a) Powder **1** (as-prepared), (b) powder **1d** (750 °C/2 h), and (c) powder **1** after keeping in sunlight for 10 days at room temperature.

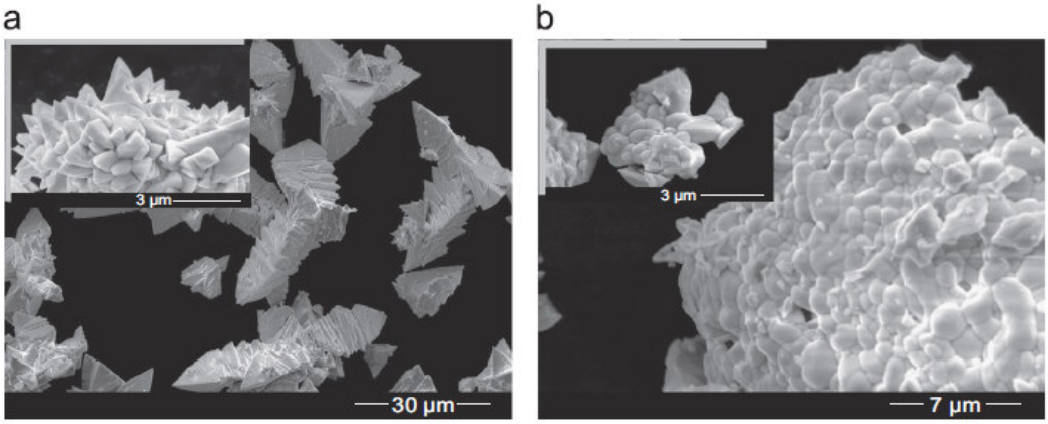

Fig. 2. SEM images of powder **1** (a) and powder **2a** (b).

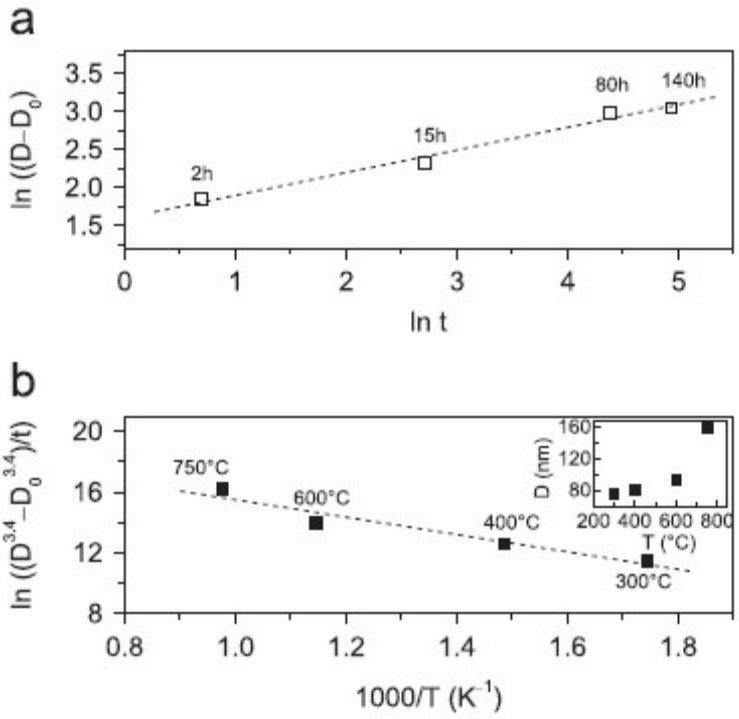

Fig. 3. (a) $\ln(D-D_0)$ (crystallite size) versus $\ln t$ (annealing time) for powder **1** annealed at 400 °C. (b) Plot of $\ln((D^{3.4}-D_0^{3.4})/t)$ as a function of $1/T$ with an annealing time of 2 h.

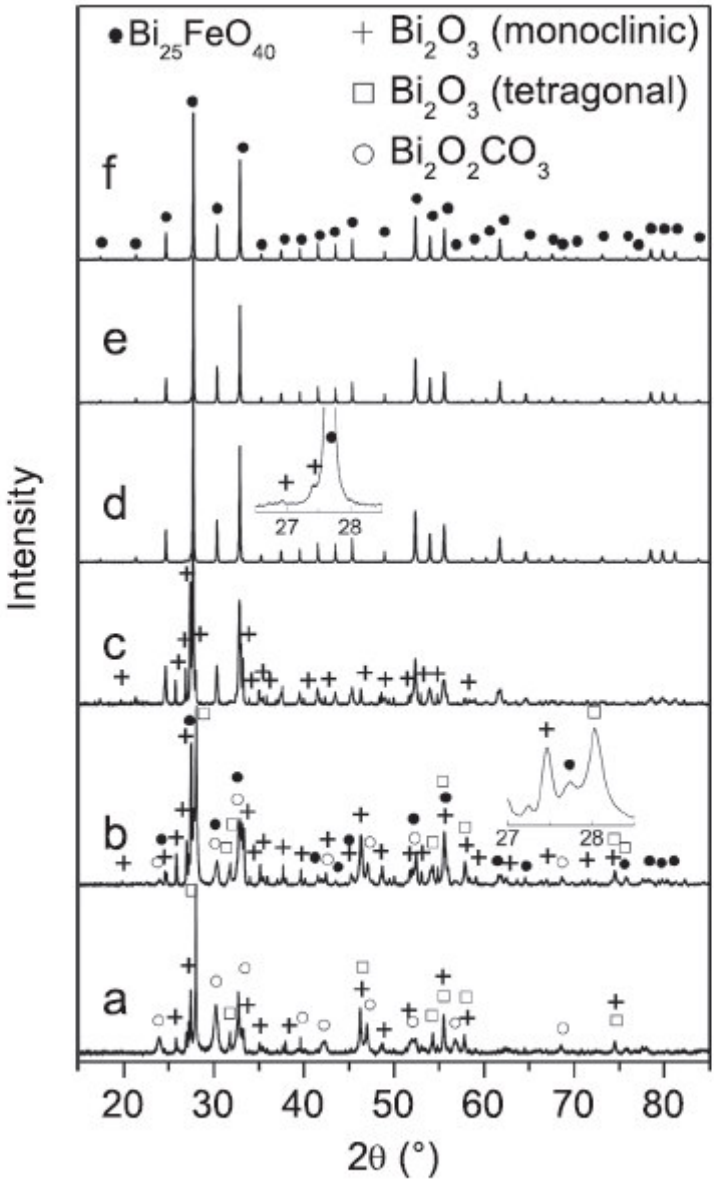

Fig. 4. Room temperature XRD patterns after calcination at various temperatures of the ($Bi_{25}Fe$)-gel (heating/cooling 5 K min^{-1}): (a) 300 °C, 2 h; (b) 400 °C, 2 h; (c) 500 °C, 2 h; (d) 750 °C, 2 h (powder **2a**); and (e) 700 °C, 10 h (powder **2b**).

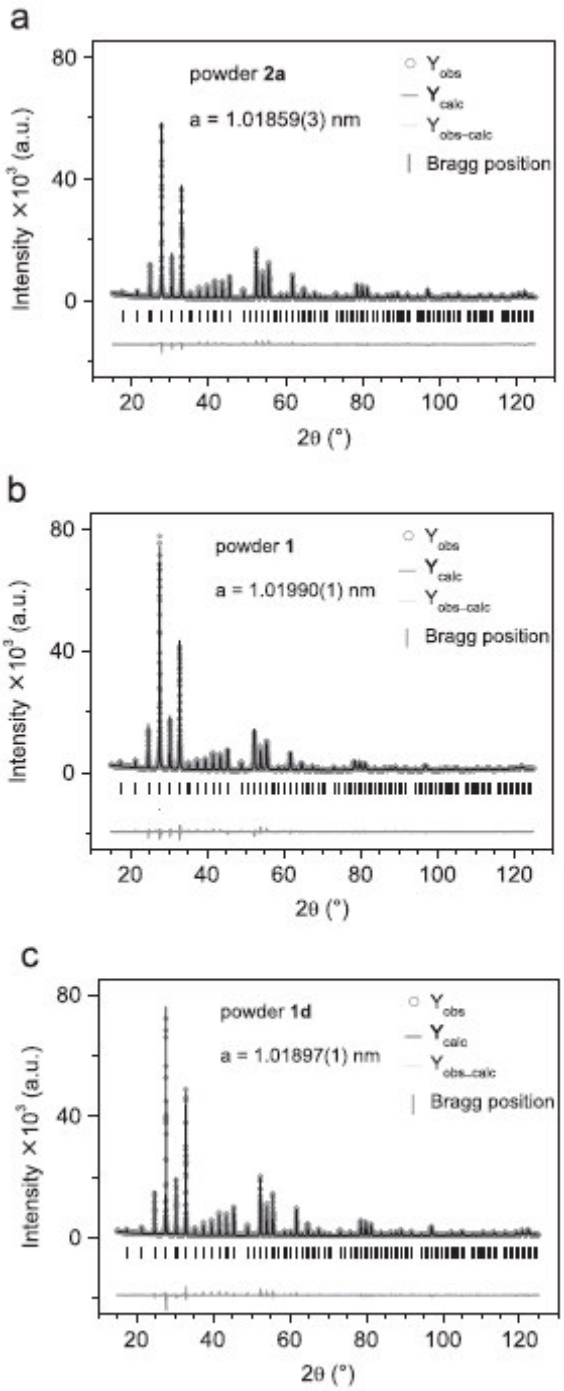

Fig. 5. Rietveld refined XRD patterns (Cu-$K_{(\alpha1+\alpha2)}$ radiation) of (a) powder **2a** (R_p=4.60%, R_{wp}=5.98%, and χ^2=4.59), (b) powder **1** (R_p=4.51%, R_{wp}=6.04%, and χ^2=5.86), and (c) powder **1d** (R_p=4.66%, R_{wp}=6.21%, and χ^2=4.95).

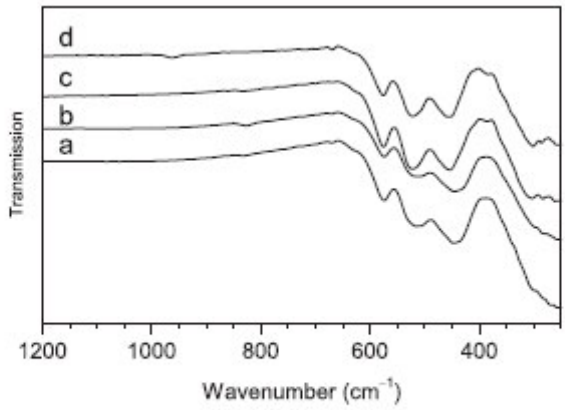

Fig. 6. FT-IR spectra (ATR technique) of (a) powder **1** (as-prepared), (b) powder **1** after keeping in sunlight for 10 days, (c) **1d** (annealed at 750 °C) and (d) powder **2a** (calcined at 750 °C).

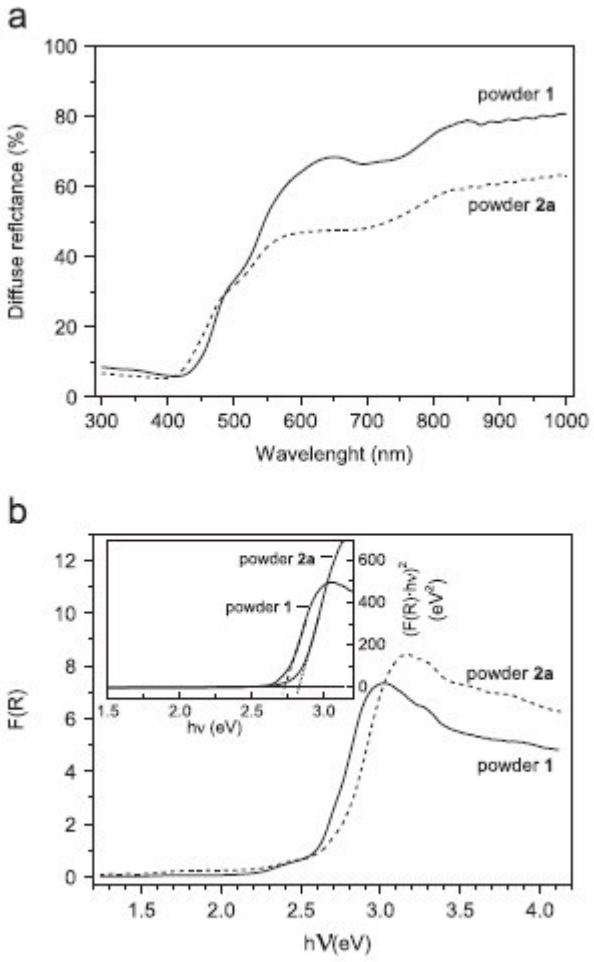

Fig. 7. (a) Diffuse reflectance spectra of powders **1** and **2a**. (b) Plot of $F(R)$ versus $h\nu$. The inset shows $(F(R)\cdot h\nu)^2$ versus $h\nu$.

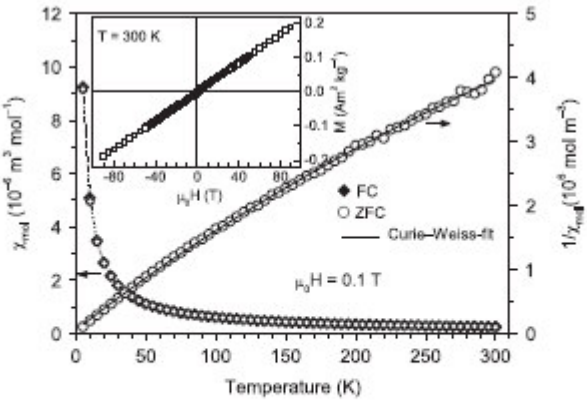

Fig. 8. Temperature dependence of the molar susceptibility for powder **2a** under zero-field cooled (ZFC) and field-cooled (FC) conditions ($\mu_0 H = 0.1$ T) in the range 5–300 K. The inset represents the magnetization (M) versus applied magnetic field (H) at 300 K.

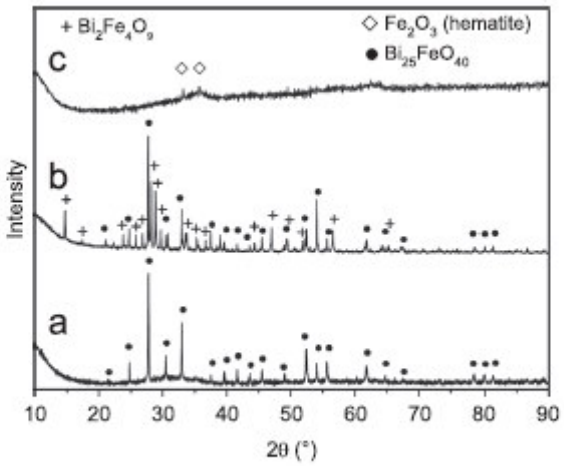

Fig. 9. Room temperature XRD pattern of the as-prepared powder **3** (a), powder **3** treated at 750 °C for 2 h (b), and powder **4** (c).

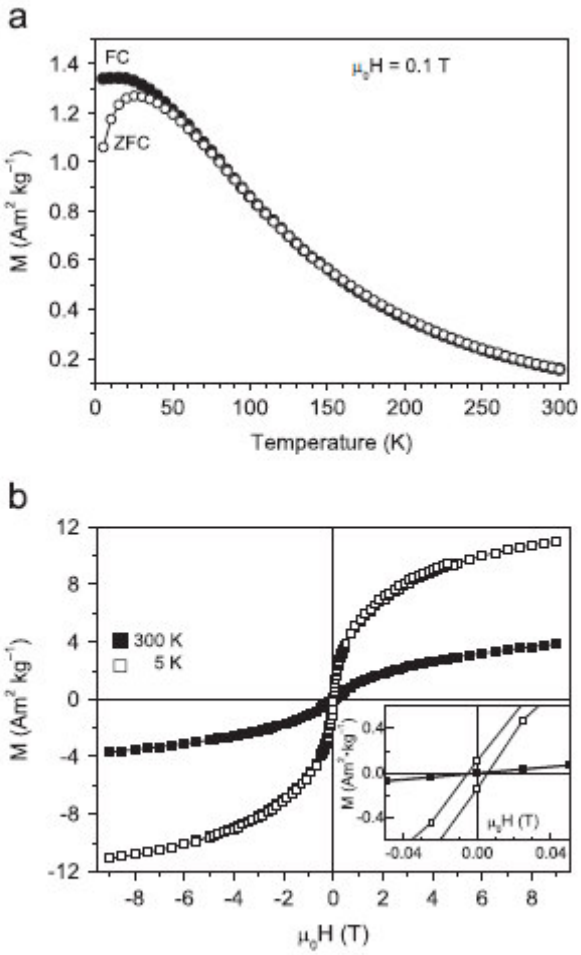

Fig. 10. (a) Temperature dependence of the magnetization for sample **3** under ZFC and FC conditions in the range 5–300 K ($\mu_0 H = 0.1$ T). (b) Magnetization (M) versus applied field (H) at 300 and 5 K.

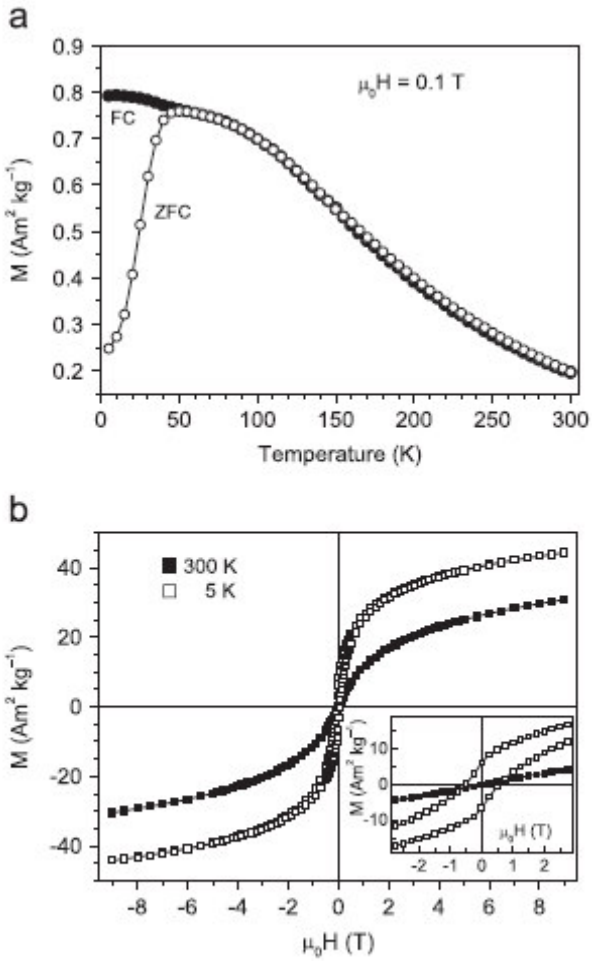

Fig. 11. (a) Temperature dependence of the magnetization for sample **4** under ZFC and FC conditions in the range 5–300 K ($\mu_0 H$ = 0.1 T). (b) Magnetization (M) versus applied field (H) at 300 and 5 K.

References

[1] M. Peltier and F. Micheron, *J. Appl. Phys.* 48 (1977) 3683–3690.

[2] L. Venturini, E.G. Spencer, A.A. Ballman, *J. Appl. Phys.* 40 (1969) 1622–1624.

[3] V. I. Chmyrev, V. M. Skorikov, E.V. Larina, *Inorg. Mater.* 42 (2006) 381–392.

[4] D.C. Craig and N.C. Stephenson, *J. Solid State Chem.* 15 (1975) 1–8.

[5] Y. Du, Z. Cheng, Z. Yu, S.X. Dou, X. Wang, L.Q. Liu, *J. Nanosci. Nanotechnol.* 12 (2012) 1684–1687.

[6] D.J. Arenas, T. Jegorel, C. Knab, L.V. Gasparov, C. Martin, D.M. Pajerowski, H. Kohno, M.W. Lufaso, *Phys. Rev.* 86 (2012) 144116.

[7] N. Rangavittal, T.N. Guru Row, C.N.R. Rao, *Eur. J. Solid State Inorg. Chem.* 31 (1994) 409–422.

[8] M. Devalette, N. Khachani, G. Meunier, P. Hagenmuller, *Mater. Lett.* 2 (1984) 318–319.

[9] J.L. Soubeyroux, M. Devalette, N. Khachani, P. Hagenmuller, *J. Solid State Chem.* 86 (1990) 59–63.

[10] Y. Wang, R. He, M. Yang, T. Wen, H. Zhang, J. Liang, Z. Lin, Y. Wang, G. Li, J. Lin, *Cryst. Eng. Comm.* 14 (2012) 1063–1068.

[11] S.F. Radaev, L.A. Muradyan, V.I. Simonov, *Acta Cryst.* B47 (1991) 1–6.

[12] S.F. Radaev, V.I. Simonov, Y.F. Kargin, V.M. Skorikov, *Eur. J. Solid State Inorg. Chem.* 29 (1992) 383–392.

[13] Y. Chen, Q. Wu, J. Zhao, *J. Alloys Compd.* 487 (2009) 599–604.

[14] Y. Sun, X. Xiong, Z. Xia, H. Liu, Y. Zhou, M. Luo, C. Wang, *Ceram. Inter.* 39 (2013) 4651–4656.

[15] G.-Q. Tan, Y.-Q. Zheng, H.-Y. Miao, A. Xia, H.-J. Ren, *J. Am. Ceram. Soc.* 95 (2012) 280–289.

[16] A. Sun, H. Chen, C. Song, F. Jiang, X. Wang, *Environ. Chem.* 32 (2013) 748–754.

[17] L. Wu, C. Dong, H. Chen, J. Yao, C. Jiang, D. Xue, *J. Am. Ceram. Soc.* 95 (2012) 3922–3927.

[18] M. Devalette, J. Darriet, M. Couzi, C. Mazeau, P. Hagenmuller, *J. Solid State Chem.* 43 (1982) 45–50.

[19] T. Elkhouni, M. Amami, A.B. Salah, *J. Supercond. Nov. Magn.* 26 (2013) 2997–3004.

[20] A.A. Zatsiupa, L.A. Bashkirov, I.O. Troyanchuk, G.S. Petrov, A.I. Galyas, L.S. Lobanovsky, S.V. Truhanov , *J. Solid State Chem.* 212 (2014) 147–150.

[21] C.Y. Zhang, H.J. Sun, W. Chen, J. Zhou, B. Li, Y.B. Wang, The 18th IEEE International Symposium on the Applications of Ferroelectrics, ISAF 2009, August 23–27, 2009, Xian, China, DOI: 10.1109/ISAF.2009.5307531.

[22] L. Jianmin, J. Song, J. Chen, S. Yu, D. Jin, J. Cheng, *MRS Proceedings* 1217 (2009) 1217-Y03-22.

[23] Y. Dai and L. Yin, *J. Alloys Compd.* 563 (2013) 80–84.

[24] A. Sun, H. Chen, C. Song, F. Jiang, X. Wang, Y. Fu, *RSC Adv.* 3 (2013) 4332–4340.

[25] M.T. Borowiec, A. Majchrowski, J. Zmija, H. Szymczak, T. Zayarniuk, E. Michalski, M. Barañski, *Proceedings of SPIE - The International Society for Optical Engineering* 5136 (2002) 26–30.

[26] R. Köferstein, *J. Alloys Compd.* 592 (2014) 324–330.

[27] T. Tong, D. Jin, J. Cheng, *MRS Proceedings* 1552 (2013) 13-1552-s12-62.

[28] Z.-W. Yu, H.-Y. Miao, G.-Q. Tan, *Cailiao Kexue yu Gongyi/Material Science and Technology*, 17 (2009) 757–760.

[29] E.-G. Jäger, K. Schöne, G. Werner, Elektrolytgleichgewichte und Elektrochemie (Arbeitsbuch 5), 4th ed. VEB Deutscher Verlag für Grundstoffindustrie, Leipzig, 1989.

[30] J. Rodriguez-Carvajal, *Physica* B192 (1993) 55–69.

[31] W. Kraus and G. Nolze, *Powder Diffr.* 13 (1998) 256–259.

[32] Th.H. De Keilser, E.J. Mittermeijer, H.C.E Rozendaal, *J. Appl. Cryst.* 16 (1983) 309–316.

[33] Program WinXPOW v1.06, Stoe & Cie GmbH, Darmstadt (1999).

[34] S. Hatscher, H. Schilder, H. Lueken, W. Urland, *Pure Appl. Chem.* 77 (2005) 497–511.

[35] PDF 2 (International Centre for Diffraction Data, Pennsylvania) 2001, $Bi_{25}FeO_{40}$ [46-416], Bi_2O_3 [71-465]$_{monoclinic}$, Bi_2O_3 [27-50]$_{tetragonal,}$ $Bi_2O_2CO_3$ [71-465], Fe_2O_3 [85-599] .

[36] W. Cun, W. Xinming, Z. Jincai, M. Bixian, S. Guoying, P. Ping′an, F. Jiamo, *J. Mater. Sci.* 37 (2002) 2989–2996.

[37] R. Köferstein, S.G. Ebbinghaus, *Solid State Ionics* 231 (2013) 43–48.

[38] C.E. Infante and B. Carrasco, *Mater. Lett.* 4 (1986) 194–197.

[39] R. Köferstein, L. Jäger, M. Zenkner, S.G. Ebbinghaus, *J. Eur. Ceram. Soc.* 29 (2009) 2317–2324.

[40] D. Hennings and S. Schreinemacher, *J. Eur. Ceram. Soc.* 9 (1992) 41–46.

[41] Y.F. Kargin and V.M. Skorikov, *Ferroelectrics* 167 (1995) 257–265.

[42] A. Maître, M. François, J.C. Gachon, *J. Phase Equilib. Diffus.* 25 (2004) 59–67.

[43] H. K. Cammenga and M. Epple, *Angew. Chem.* 107 (1995) 1284–1301.

[44] P. Kubelka and F. Munk, *Z. Techn. Phys.* 11 (1931) 593–601.

[45] G. Kortüm and J. Vogel, *Z. Phys. Chem.* 18 (1958) 110–122.

[46] S.M. Sze, Physics of Semiconductor Devices, J. Wiley & Sons, 1969, p. 52.

[47] D. Senuliene, E. Babonas, E.I. Leonov, I. Muminov, V.M. Orlov, *Fizika Tverdogo Tela* 26 (1984) 1281–1284.

[48] M.T. Borowiec, Int. IX School Phys. Appl. Sing. Cryst. Liq. Cryst., Jurata 1990, p.II, pp. 224–228, 1990.

[49] M. Nowak, B. Kauch, P. Szperlich, *Rev. Sci. Instrum.* 80 (2009) 046107.

[50] A. Arrott, *J. Appl. Phys.* 29 (1958) 508–512.

[51] C.P. Bean and J.D. Livingston, *J. Appl. Phys.* 30 (1959) 120S–129S.

[52] T.P. Raming, A.J.A. Winnubst, C.M. van Kats, A.P. Philipse, *J. Colloid Interface Sci.* 249 (2002) 346–350.

[53] L.D. Tung, V. Kolesnichenko, D. Caruntu, N.H. Chou, C.J. O'Connor, L. Spinu, *J. Appl. Phys.* 93 (2003) 7486–7488.

[54] R. Köferstein, T. Walther, D. Hesse, S.G. Ebbinghaus, *J. Mater. Sci.* 48 (2013) 6509–6518.

[55] R. Zboril, L. Machala, M. Mashlan, J. Tucek, R. Muller, O. Schneeweiss, *phys. stat. sol.* 1 (2004) 3710–3716.

[56] M.M. Ibrahim, G. Edwards, M.S. Seehra, B. Ganguly, G.P. Huffman, *J. Appl. Phys.* 75 (1994) 5873–5875.

[57] F. Bødker and S. Mørup, *Europhys. Lett.* 52 (2000) 217–223.

[58] C. Cannas, G. Concas, D. Gatteschi, A. Falqui, A. Musinu, G. Piccaluga, C. Sangregorio, G. Spano, *Phys. Chem. Chem. Phys.* 3 (2001) 832–838.